Investigation of the Nanoscale Morphology in Industrially Relevant Clearcoats of Waterborne Polymer Colloids by Means of Variable-Angle-Grazing Incidence Small-Angle X-ray Scattering

Vagias, Apostolos; Chen, Qi; ten Brink, Gert H.; Hermida-Merino, Daniel; Scheerder, Jurgen; Portale, Giuseppe

Published in:
ACS Applied Polymer Materials

DOI:
10.1021/acsapm.9b00601

Publication date:
2019

ACS APPLIED POLYMER MATERIALS

Article

Cite This: ACS Appl. Polym. Mater. 2019, 1, 2482−2494

pubs.acs.org/acsapm

Investigation of the Nanoscale Morphology in Industrially Relevant Clearcoats of Waterborne Polymer Colloids by Means of Variable-Angle Grazing Incidence Small-Angle X-ray Scattering

Apostolos Vagias,[†,‡] Qi Chen,[∥] Gert H. ten Brink,[§] Daniel Hermida-Merino,[⊥] Jurgen Scheerder,[∥] and Giuseppe Portale*[,†,‡]

[†]Dutch Polymer Institute (DPI), P.O. Box 902, 5600 AX Eindhoven, The Netherlands

[‡]Macromolecular Chemistry and New Polymeric Materials Group, Zernike Institute for Advanced Materials, and [§]Zernike Institute for Advanced Materials, University of Groningen, Nijenborgh 4, 9747 AG Groningen, The Netherlands

[∥]DSM Coating Resins B.V. Sluisweg 12, Waalwijk 5145 PE, The Netherlands

[⊥]DUBBLE Beamline at the ESRF, Netherlands Organization for Scientific Research, 71 Avenue des Martyrs, CS40220, 38043 Grenoble, France

Supporting Information

ABSTRACT: Soft polymer colloidal water suspensions are extremely important formulations for industrial applications such as water-based environmental-friendly coatings, paints, and adhesives. Homogeneity of the final coating at the micrometer and nanoscale is a crucial factor for optimal coating performance, such as barrier properties against solvent permeation. Here, we investigated the remnant nanostructure in slot-die-coated micrometer-sized thick clear coating films (clearcoats) of three different waterborne polymer colloids (pure soft, pure hard, and soft/hard multiphase), commonly utilized as primers in paint formulations [Mader et al. *Prog. Org. Coat.* **2011**, *71*, 123−135], using variable-angle grazing incidence small-angle X-ray scattering (GISAXS) complemented with cross-sectional atomic force microscopy (cs-AFM). After complete macroscopic drying, the coating films exhibit the presence of residual nanostructure with characteristic distance (d^*) smaller than the original particle size and even smaller ($\ll d^*$) heterogeneity dimensions. These nanostructural heterogeneities (i) develop due to partial particle coalescence, (ii) are preferentially located close to the air−film interface and (iii) demonstrate the tendency to align perpendicular to the air−film interface, implying vertical gradient in hydroplasticization effects having occurred earlier during film formation. The extent and size of the nanostructural heterogeneities, driven by the slot-die coating application, strongly depend on the polymer chemistry (glass transition temperature, T_g) and the colloidal architecture. Last, solvent exposure has a significant impact on the nanostructure, causing the removal of these heterogeneities and leading to a more strongly coalesced film.

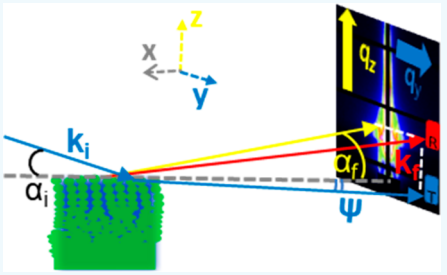

KEYWORDS: *waterborne polymer coatings, acrylics, slot-die coating, variable-angle GISAXS, nanostructure, annealing, AFM, glass transition*

INTRODUCTION

Waterborne polymer colloids are increasingly utilized as main components in resin formulations for paint applications, barrier coatings, and anticorrosion products due to the reduced environmental and health hazards compared to solvent-based resins.[2−6] However, the distribution of colloids as a dispersed phase becomes challenging when using water as solvent.[2,7] A number of microscale defects can develop during film drying.[3,8] The interplay between the glass transition temperature (T_g) of the colloids and the drying temperature, as well as the size distribution of polymer colloids, can have a crucial impact on the film's structure and mechanical properties including the lateral and vertical segregation of nanostructural features within the coating.[7,9,10] Elucidating how variabilities in waterborne polymer colloids, such as T_g, molecular weight, chemical composition, and colloidal architecture, can influence the film structure is key in optimizing the final properties of waterborne coatings.[11] Ideally, an optimal clearcoat film for paint and protective coating applications (e.g., clearcoats/topcoats) should be free of defects, minimize the impact of plasticizing agents such as water and ethanol, exhibit strong anticorrosive and solvent barrier properties,[12] and demonstrate significant resistance against "weathering effects"[13] when exposed to outdoor environment. To achieve these features, a clearcoat needs to balance between facile deformability/spreadability (low T_g) and high mechanical strength (high T_g).[11,14] It is thus mandatory to noninvasively inspect the possible presence of nanostructural heterogeneities in micro-

Received: June 30, 2019
Accepted: August 23, 2019
Published: August 23, 2019

DOI: 10.1021/acsapm.9b00601
ACS Appl. Polym. Mater. 2019, 1, 2482−2494

meter-sized thick coatings and to investigate the influence of particle composition and architecture on those heterogeneities.

The currently established drying mechanism of waterborne latex suspensions involves the following stages:[2,7] close packing, deformation, and chain interdiffusion. The film formation involves the competitive interaction between rate of water loss (convection), diffusion of polymer colloids, interfacial tension, capillary forces, and latex suspension's (low-shear) viscosity. Imperfections arising during the packing and deformation stages could affect the coating structure.[15,16] Two types of constituents have been frequently assigned to heterogeneities: water[17−19] and surfactant stabilizers.[9,16,20−23] While information about the presence of water "pockets" in coatings from soft ($T_{\text{film formation}} > T_g$) polymer colloids within the submicrometer range has been reported,[24] quantification about the exact characteristic length scales (distance and the size) of such heterogeneities is less available. To study the existence and the distribution of submicrometric heterogeneities, one should aim at characterization techniques with broad spatial resolution, high surface sensitivity, and the possibility to probe buried features. With spatial resolution of a few nanometers, AFM can probe only the upper coating surface, while electron microscopy-based methods can be destructive and under circumstances artifacts could be inevitable. Moreover, the aforementioned local methods do not allow for sufficient statistics over the whole sample. Small-angle X-ray (SAXS) and small-angle neutron scattering (SANS) techniques are optimal for characterizing particle morphology in polymer colloidal suspensions.[25−27] These techniques have been also used to probe nanostructural heterogeneities in free-standing films either of hard, nondeformable polymer colloids[28−31] or for soft, deformable polymer colloids.[32−34] Slot-die coating is the key deposition method for application-relevant coatings (e.g., paint brushing or varnish application treatments). It involves the deposition of a liquid formulation onto a substrate toward a controllable and uniform final film thickness.[35] It is thus highly valuable to inspect the structure of coating films obtained by using slot-die coating, as a function of colloid softness, directly in their supported form without any further modifications. These technical challenges can be bypassed using grazing incidence small-angle X-ray scattering (GISAXS), where the use of a 2D detector allows probing structural variations with spatial resolution between 1 and 1000 nm simultaneously in the film plane and out-of-plane.[36,37] While GISAXS is a well-established and powerful technique to study nanostructure in submicrometrically thin films,[38−41] to the best of our knowledge it has rarely been utilized to study much thicker films (thickness of several micrometers), with the exception of one case on diblock copolymer films.[42] Thicknesses between 1 and well above 10 μm are commonly utilized for real applications such as waterborne polymer clearcoats (e.g., top-coating primers).[43]

In this study, we employ GISAXS to monitor the in-plane and out-of-plane order in the film nanostructure of industrially relevant waterborne coatings. These coatings are made of latex polyacrylic nanoparticles with an approximate particle size of 100 nm. The waterborne coatings in this work are used as clearcoats (clear finishes) for wood furniture, doors, and joinery (window and door frames) as well as paint primers,[43] their main function being to protect the substrates from exposure to liquids such as water, coffee, and red wine (e.g., alcohol). Our goal is threefold: (1) to inspect and quantify the distribution of nanostructured heterogeneities within the film, (2) to assess the influence of particle softness and architecture on those heterogeneities, and (3) to study the correlation between coating nanostructure and coating barrier properties. Synergizing structural information obtained from GISAXS with complementary cross-sectional AFM results, our work proposes a robust protocol to inspect the distribution of nanometer-sized spatial heterogeneities across the film and perpendicular to its surface.

MATERIALS AND METHODS

Synthetic Procedure. Three different polymer colloidal particles were prepared by semicontinuous emulsion polymerization and named "S", "H", and "HS", depending on their glass transition (see Table 2). The following chemicals were used as supplied. *n*-Butyl methacrylate (*n*-BMA), *n*-butyl acrylate (*n*-BA), methyl methacrylate (MMA), and acrylic acid (AA) (Dow Chemical Company) were used as monomers. Ammonium persulfate (United Initiators GmbH) was used as initiator. Sodium bicarbonate and ammonia (Innophos and Brenntag Nederland B.V.) were used to regulate the pH. Rhodafac RS/710E-30 (Solvay) was used as emulsifier. Proxel Ultra10 (Arch UK Biocides Ltd.) is added as preservative. The synthesis of the single-phase S and H particles is comprised of three steps, while one extra step is required for the HS particles.

Step 1. A 2000 cm^3 flask equipped with a thermometer, a N_2 inlet, and an overhead stirrer was charged with demineralized water (685.9 g), sodium bicarbonate (0.4 g), ammonia (0.8 g, 25 wt % solution), and Rhodafac RS/710E-30 (27.6 g). A first emulsified monomer feed, specific for each formulation, was prepared in feeding funnels according to Table 1.

Table 1. Composition of the Examined PA-Based Materials (All Values in grams)

	S	H	HS
n-butyl methacrylate (*n*-BMA)	428.7	169.3	300.0
n-butyl acrylate (*n*-BA)	200.5		140.3
methyl methacrylate (MMA)	37.5	497.3	26.3
acrylic acid (AA)	35.1	35.1	24.6
sodium bicarbonate	0.5	0.5	0.2
Rhodafac RS/710E-30	15.3	15.3	8.1
demineralized water	236.0	236.0	165.2

Step 2. For each formulation, a glass reactor was charged with a solution of ammonium persulfate (2.1 g), sodium bicarbonate (0.1 g), and Rhodafac RS/710E-30 (4.8 g) in demineralized water (42.9 g) and was heated to T = 85 °C. Once 85 °C was reached, 5 wt % of the first monomer feed was added, followed by the addition of an ammonium persulfate solution (0.4 g for "HS", 0.4 g for "H", and 2.1 g "HS" in 4.7 g of demineralized water). The reaction was first allowed to reach the peak temperature ($T \sim$ 89 °C), and then the rest of the first monomer feed was added in 120 min for "HS" and in 180 min for both "S" and "H". After the feeding period, the reaction mixture was left to react further at T = 85 °C for another 45 min.

Step 3 (Only for HS). A second emulsified monomer feed was prepared by mixing *n*-butyl methacrylate (*n*-BMA, 50.8 g), methyl methacrylate (MMA, 149.2 g), acrylic acid (AA, 10.5 g), sodium bicarbonate (0.3 g), Rhodafac RS/710E-30 (7.2 g), and demineralized water (94.3 g) until a stable monomer feed was obtained. After the 45 min holding period, this second monomer feed was added in 60 min together with the remainder of the ammonium persulfate solution, and the reaction mixture was left to react at T = 85 °C for another 30 min.

Step 4. The reaction mixture was allowed to cool to T = 23 °C, the pH was adjusted by adding a dilute ammonia solution (≈4 wt %), and Proxel Ultra10 was added (5.0 g). The solid content was measured by using a Mettler Toledo HB-43S moisture analyzer using 105 °C as drying temperature and was adjusted to 39 wt % by addition of

DOI: 10.1021/acsapm.9b00601
ACS Appl. Polym. Mater. 2019, 1, 2482−2494

demineralized water. Finally, the batch was filtered over a 75 μm cloth and collected. The conversion was measured by GC and was >99.9%.

Formulation Characterization. The sample glass transition (T_g) was measured by differential scanning calorimetry (DSC). Thermal transitions of the synthesized formulations are reported in Figure S1, and associated parameters (T_g and C_p) per formulation are summarized in both Table 2 and Table S1. The relevant physical properties for each formulation are summarized in Table 2. The particle size was measured by dynamic light scattering (DLS), and the size distribution was evaluated by using the CONTIN algorithm. A TEM image for the HS particles is reported in Figure S2. The particle size and architecture were also studied by solution small-angle X-ray scattering (SAXS) experiments (Figure 1 and Figure S3). SAXS was performed at the MINA diffractometer of the University of Groningen, equipped with a Cu rotating anode (X-ray wavelength λ = 1.5413 Å/energy of 8 keV) and using a Bruker Vantec 2000 2D detector placed 3 m away from the sample. An amount of 70 μL of each suspension was loaded into a 1.5 mm thick glass capillary. The capillary was flame-sealed to prevent water evaporation, and the exposure time was of the order of 10–30 min depending on the polymer concentration. SAXS images were normalized by the exposure time and were integrated by using the Fit2D software. The scattering angles 2θ were calibrated using the position of known diffraction peaks from a standard silver behenate powder, and the SAXS intensity was finally reported as a function of the modulus of the scattering vector $q = (4\pi/\lambda) \sin \theta$.

Table 2. Main Physical Properties of the Examined PA-Based Materials

property	HS (hard–soft)	S (soft)	H (hard)
solid content (%)	39.0	39.1	39.1
pH	7.0	6.8	8.1
particle radius by DLS, R (nm)	53 ± 2	54 ± 1	50 ± 2
T_g, midpoint (°C)	4.6 and 96.1	5.0	94.9
C_p [J g^{-1} °C^{-1}]	0.20 and 0.08	0.29	0.32

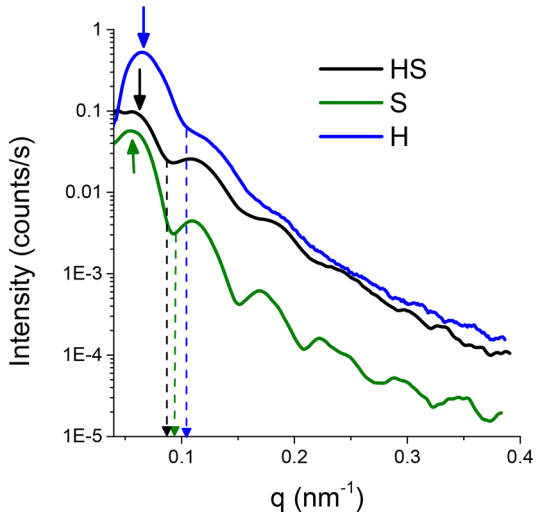

Figure 1. SAXS intensity curves normalized with respect to the acquisition time, $I(q)$ (counts s^{-1}), vs wavevector q (nm^{-1}) for aqueous suspensions of the different formulations at 39 wt % solid content: HS (black), S (green), and H (blue). The vertical dashed-dotted arrows point to the first minima position of the particle form factor, and the short solid arrows denote the peak position q^* from the structure factor $S(q)$ for each color-matching curve.

Film Preparation. Films were prepared at T = 23 °C by slot-die coating onto sodalime glass slides (75 mm × 25 mm dimensions, Menzel). An amount of 160 μL from aqueous HS, S, and H suspensions was coated on the glass by using aluminum slot dies with different gap clearances (10 and 120 μm), and different starting polymer concentrations in water were used to achieve different uniform film thicknesses (Figure S4). Water evaporation was been studied by recording the weight loss of the different HS, S, and H samples over time (Figure S5).

Film Characterization. *Atomic Force Microscopy (AFM) Imaging.* AFM measurements were performed in at least three dry films per colloidal formulation and at three different locations per film separated by several micrometers one from each other. AFM topography images were acquired at the film–air interface, with a NanoScope V multimode atomic force microscope (Bruker Nano Surfaces, Santa Barbara, CA) using silicon cantilevers with resonance frequencies of 300–400 kHz (model: TESP, Bruker Nano surfaces).

AFM Imaging of Coating Cross Section (cs-AFM). The cross section of the HS coating, applied on thin (150 μm) borosilicate glass slide, was prepared by using a Leica EM TIC3X ion beam milling system by exposing the cross section to argon ions with acceleration voltage of 4 kV and gun current of 1.6 mA for 8 h under ambient temperature. We prepared one single HS sample using a triple-ion beam miller. The milled area was ~5 mm × 0.5 mm (the total thickness of the glass slide + coating). The ion beam milled sample was mounted onto an AFM vertical sample holder. The cs-AFM images were obtained under ambient conditions in tapping mode with a NanoScope V multimode atomic force microscope (Bruker Nano Surfaces, Santa Barbara, CA) using silicon cantilevers with resonance frequencies of 300–400 kHz (model: TESP, Bruker Nano surfaces). In addition, a single noncolloidal-based atactic polystyrene film was prepared and characterized by cs-AFM. PS with 370K molecular weight (Polymer Source Inc.) was spin-coated under 400 rpm for 60 s from a 6 wt % toluene solution and annealed at T (= 140 °C) > $T_{g,PS}$ (~100 °C)[44] for 1 h to repair defects stemming from spin-coating. The roughness of the analyzed cross sections was determined from 10 different randomly selected areas (2 μm × 2 μm) at the same depth. In total, micrographs at eight different depths from the air–film interface have been acquired.

Grazing Incidence X-ray Scattering (GISAXS). GISAXS experiments were conducted at T = 23 °C, between 2 and 4 days following film preparation, at the Dutch-Belgian beamline (DUBBLE, BM26B) at the ESRF, Grenoble, using 12 keV irradiation energy (λ = 1.033 Å).[45,46] In total, at least three different films per colloidal formulation (H, S, and HS) have been examined. The X-ray beam was focused at the sample position and had dimensions of about 300 μm (perpendicular to the film surface) × 1000 μm (along the film surface). To resolve scattering features of the relevant morphologies in the examined systems, we used a sample-to-detector distance (S-to-D) of 7 m. The GISAXS 2D patterns were recorded on a noiseless, solid-state Pilatus 1M Dectris detector, with 981 (laterally) × 1043 (vertically) pixels and pixel size of 172 μm × 172 μm as a function of q_y and q_z (the component q_x along the beam direction can be neglected here). The moduli of the in-plane and out-of-plane scattering wavevectors are respectively

$$q_y = \left(\frac{2\pi}{\lambda}\right) \cos(\alpha_f) \sin(\psi) \quad (1)$$

$$q_z = \left(\frac{2\pi}{\lambda}\right)[\sin(\alpha_f) + \sin(\alpha_i)] \quad (2)$$

where ψ is the in-plane scattering angle in the direction parallel to the film surface, α_i is the incident angle of the X-ray beam, and α_f is the exit scattering angle in the vertical direction perpendicular to the film surface. The full measured in-plane range was q_y = 0.02–1.7 nm^{-1} (i.e., 4–290 nm), and the out-of-plane one was up to q_z = 1.3 nm^{-1}. Note that the GISAXS patterns presented in this article are a zoomed-in view of the larger acquired patterns. All the acquired GISAXS patterns have been normalized for the incoming beam intensity. The nominal critical angles α_c of the polymer films and of the sodalime glass substrate are ~0.1°–0.11° and 0.15°, respectively. The sample surface was aligned with respect to the beam direction by using a

DOI: 10.1021/acsapm.9b00601
ACS Appl. Polym. Mater. 2019, 1, 2482–2494

high-resolution HUBER circular segment goniometer. The estimated error on α_i was ±0.05° (as determined from the uncertainty in calculating the center of the transmitted beam profile scans from the photodiode embedded in the beamstop and the position of the reflected X-ray beam on the detector). The incident angle α_i was varied from close to ($\alpha_i \sim \alpha_c$) to well above ($\alpha_i > \alpha_c$) the critical angle α_c of the polymer to probe the sample nanostructure at different distances starting from close to the air−film interface down to the glass substrate. The total accumulation time for each α_i was 300 s. Because of the particular nature of the examined films (waviness at the film−air interface and relatively thick, micrometer-sized films), the transmitted scattering signal increases over the reflected one, and the Yoneda[47] peak appears broadened along q_z. Because of this broadening, the $I(q_y)$ vs q_y intensity cuts have been better computed at q_z positions slightly higher than the position of the Yoneda peak height (e.g., up to 20−30 pixels above the Yoneda peak position) to more clearly observe the scattering peaks. The horizontal cuts have been obtained by averaging the intensity of ±5 adjacent rows along the q_z-axis ($\Delta\alpha_f = 0.012°$).

RESULTS AND DISCUSSION

The water-based colloidal suspensions of each formulation have been first characterized by transmission SAXS (Figure 1). The SAXS curves for the three different colloidal suspensions show several oscillations at high q values typical for the particle form factor together with a peak in the region $q < 0.1$ nm^{-1}.[48] The position of the scattering minima matches the one expected for spherical particles.

The minima are damped due to polydispersity in particle size, denoted here as $\sigma_{rel} = \sigma/\bar{R}$, with σ being the standard deviation of the particle size distribution function (Schulz−Zimm in this case). Analysis of the first minimum position and fitting of the SAXS curves (Figure S3 and Table S2) provides the following spherical particle radii $R_{p,S} = 50$ nm ($\sigma_{rel} = 0.07$), $R_{p,H} = 45$ nm ($\sigma_{rel} = 0.15$), and $R_{p,HS} = 46$ nm ($\sigma_{rel} = 0.16$), slightly smaller than the DLS results reported in Table 2. Such a discrepancy is often reported between these two methods.[49] The TEM micrograph for HS particles (Figure S2) confirms the size polydispersity observed by SAXS. Interestingly, while the SAXS curves of the pure H and S suspensions can be successfully described by using a simple homogeneous sphere model, the SAXS curve for the multiphase HS required the use of a two-phase model (see Figure S3 and "SAXS Modeling of Suspension Data" section in the Supporting Information). The HS particle form factor can be well described by a concentric core−shell spherical model (details provided in the Supporting Information). The remaining minor discrepancies between the modeled curve and the experimental data could be attributed to several reasons such as deviation from a spherical shape, incorrect assumption of the size distribution function, inhomogeneities in the polymer shell, or the presence of a surfactant corona, not considered here. The scattering peaks located at q^* is generated by the maximum of the structure factor describing the spatial correlation among particles and is related to the average interparticle distance ($d_{interparticle} = 2\pi/q^*$).[48] Variability of the interparticle distance in suspensions ($d_{interparticle,H} = 94$ nm < $d_{interparticle,S} = 115$ nm < $d_{interparticle,HS} = 125$ nm) may probably reflect differences in the extent of interparticle interactions stemming from pH variations (Table 2) or differences in the relative amounts of (charged) surfactant stabilizer and ionization degrees of different weak organic polyacids.[49,50]

By use of slot-die coating, the deposition of high-quality coating films with controlled thickness and high homogeneity along the in-plane direction has been mastered (Figure S4). SEM images show the achieved uniformity in both film thickness and topography (see Figure S5). The thickness closely relates to the thickness of single layer of paintbrush coatings.[51,52] A detailed stylus profilometry study suggested a root-mean-squared waviness $W_q = 1.5$ μm for such thick films and showed that thickness nonuniformities at the film edges are present, but their contribution is very limited as they represent not more than 15% of the total film width distributed on the two edges (Figure S5). The availability of such good quality films is fundamental for the GISAXS study presented here.

AFM images acquired on the surface of ∼30 μm thick films are reported in Figure 2 and suggest partially coalesced

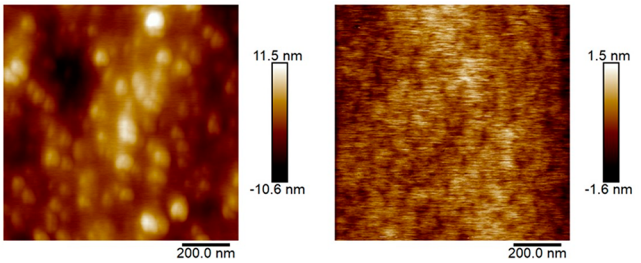

Figure 2. AFM height topography 1 μm × 1 μm images: HS (left panel) and S (right panel) films.

particles in the case of HS film with a root-mean-square roughness $R_{q,HS} = 2.6 \pm 0.4$ nm, about 4 times larger than for films of the soft S analogue, $R_{q,S} = 0.6 \pm 0.3$ nm.

AFM has an excellent spatial resolution but is limited only to topography information at the air−film interface. To probe the nanostructure close to the air−film interface as well as within the film and across the film thickness, we utilized variable-angle GISAXS analysis. GISAXS is a powerful technique to study a variety of structures found in supported thin films.[37,53] Its application to thick (>1 μm) films is more challenging but still possible. Tuning the incidence angle (α_i) of the X-rays with respect to the sample surface allows one to change the X-ray penetration depth (ξ_p) inside the film.[42] This approach was efficiently used in the past to obtain depth-resolved structural information by using GISAXS on block copolymer thick films and carbon-based/nanoparticle films.[54−56] For a given sample with X-ray refractive index $n = 1 - \delta - i\beta$, the penetration depth ξ_p (depth at which the beam intensity is attenuated by 1/e) depends on the material's critical angle ($\alpha_c = \sqrt{2\delta}$), the X-ray wavelength (energy of the X-ray photons), and the incident angle α_i (eq S7). Typical $\xi_p(\alpha_i)$ vs α_i curves computed for polyacrylic-based films that closely represent the composition of our coatings at an X-ray energy of $E = 12$ keV are plotted in Figure S6. The calculated values for $\xi_p(\alpha_i)$ show that in principle, depending on α_i, the ξ_p can be tuned from about 5−10 nm up to tens of micrometers. However, it should be considered that the presence of surface defects, surface undulations, and menisci limits the accuracy in the determination of α_i and hinders the precise calculation of ξ_p, especially at low α_i. This is particularly true for thick polymer films as the ones used here. Thus, the actual minimum penetration depth at $\alpha_i \approx \alpha_c$ is expected to be well above 10 nm, and the ξ_p values for $\alpha_i > \alpha_c$ mentioned here should be considered as nominal values for the intended depth resolution. Moreover, as hard X-rays ($E > 6$ keV) were used, ξ_p increases quite rapidly for $\alpha_i > \alpha_c$. Thus, it is quite difficult

DOI: 10.1021/acsapm.9b00601
ACS Appl. Polym. Mater. 2019, 1, 2482−2494

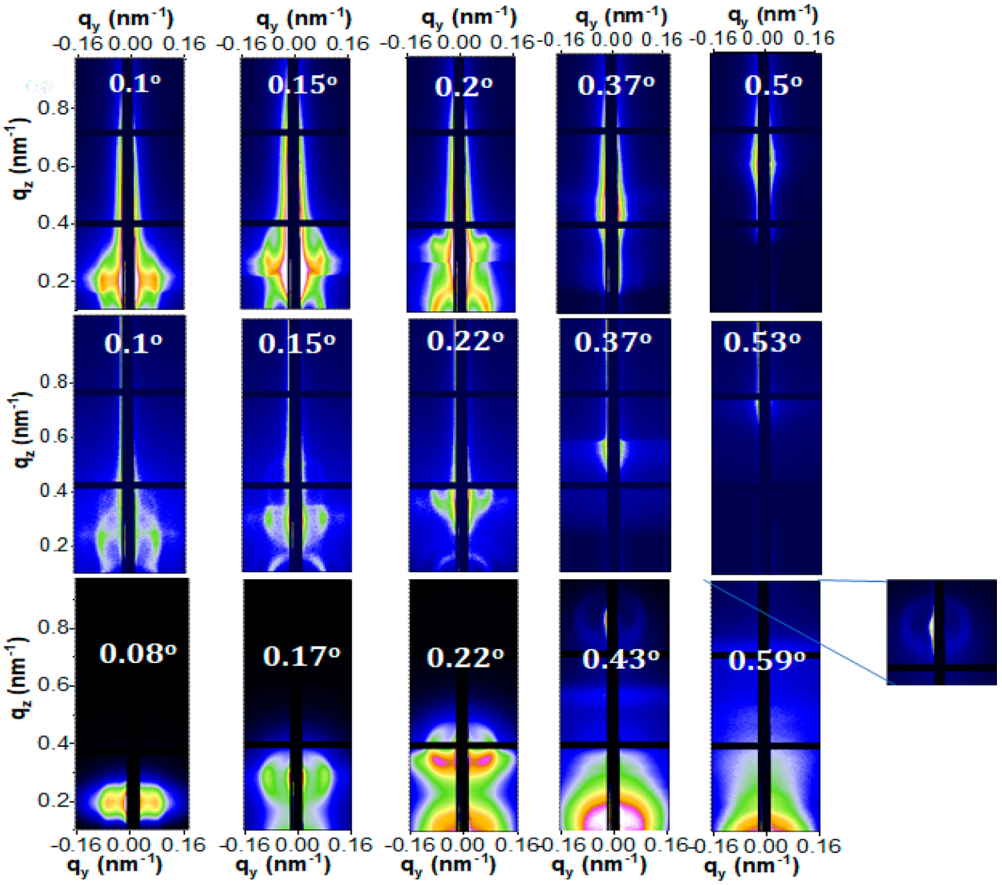

Figure 3. GISAXS patterns as a function of incident angle α_i for the different films slot die coated on sodalime glass substrates: HS (top row); S (middle row); H (bottom row). The intensity scales as follows: from 0 to 7×10^{-4} (HS), 0 to 5×10^{-4} (S) and then for (H), from 0 to 2×10^{-1} ($\alpha_i = 0.08°$; $\alpha_i = 0.17°$), 0 to 5×10^{-2} ($\alpha_i = 0.22°$), 0 to 10^{-2} ($\alpha_i = 0.43°$) and 0 to 2×10^{-3} ($\alpha_i = 0.59°$). At the lowest row ($\alpha_i = 0.59°$, H coatings), the specular signal is shown to the side as it was present at higher q_z than the one displayed for all the other scattering patterns. Concerning HS and S coatings, the nominal penetration depth values ($\xi_p(\alpha_i)$) associated with the used incident angles (α_i) are ~10 nm ($\alpha_i = 0.1°$); ~10 μm ($\alpha_i = 0.15°$); ~13 μm ($\alpha_i = 0.17°$); ~16 μm ($\alpha_i = 0.2°$); ~19 μm ($\alpha_i = 0.22°$); ~35 μm ($\alpha_i = 0.37°$); ~47 μm ($\alpha_i = 0.5°$); ~50 μm ($\alpha_i = 0.53°$). Similarly, for H coatings: 6 nm ($\alpha_i = 0.08°$); 11 μm ($\alpha_i = 0.17°$); 16 μm ($\alpha_i = 0.22°$); ~35 μm ($\alpha_i = 0.43°$); ~45 μm ($\alpha_i = 0.59°$).

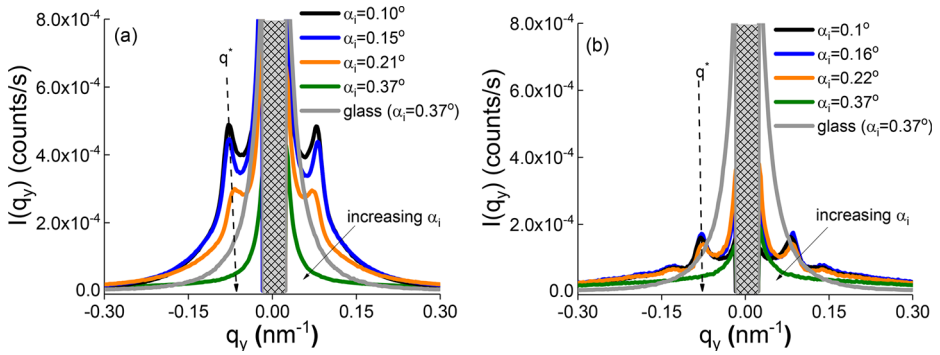

Figure 4. Intensity cuts $I(q_y)$ (counts s^{-1}) vs q_y for (a) the HS and (b) the S films as a function of α_i. The cuts stem from the GISAXS scattering patterns of the respective films on sodalime glass substrates. The solid arrow points to the direction of increasing (α_i), and the dashed arrow points to the peak position $q^*(\alpha_i)$ of the characteristic correlation length, $d^*(\alpha_i)$. The gray-shaded rectangular region denotes the beamstop position.

to fine-tune ξ_p in the range from 20 nm to 1−2 μm. We have thus acquired GISAXS data at $\alpha_i \leq \alpha_c$ ($\alpha_{c,H} = 0.11°$; $\alpha_{c,HS} = \alpha_{c,S} = 0.105°$) and well above it ($\alpha_i > 0.15°$). Figure 3 shows a collection of the GISAXS patterns as a function of increasing α_i for the three investigated coatings with similar thickness ($h \sim 30$ μm).

The characteristic features present in such GISAXS patterns are explained in detail in Figure S7. First, the GISAXS results for the multiphase HS film (Figure 3, top row) are discussed. A strong change on both the pattern appearance and the scattering intensity is observed with increasing α_i. For $\alpha_i \approx \alpha_c = 0.1°$, the GISAXS pattern shows two clear symmetric anisotropic scattering signals with respect to $q_y = 0$ nm^{-1}. As expected, the intensity of these signals is enhanced close to the Yoneda peak position along the q_z direction.[47,57] The signal intensity decreases significantly with increasing α_i. Interest-

DOI: 10.1021/acsapm.9b00601
ACS Appl. Polym. Mater. 2019, 1, 2482−2494

ingly, for α_i > 0.25°, the scattering peaks are not visible anymore. Moreover, edge effects on GISAXS scattering patterns (Figure S8, shown for HS) can be neglected. Although with lower scattered intensity by ca. 6 times, the GISAXS patterns for the soft S film (Figure 3, middle row) show the same trend with increasing α_i. In contrast to the multiphase HS and to the soft S films, the GISAXS patterns from the nonfilm forming hard H colloidal formulation (Figure 3, lower row) exhibit strong scattering signal at all α_i. As a consequence of the hard colloidal particle nature, the qualitative aspects of the GISAXS patterns for the H films resemble closely the ones for polydisperse uncoalesced colloidal spheres.[58,59] To quantitatively analyze the GISAXS patterns, we performed horizontal cuts of the scattered intensity $I(q_y)$ along the in-plane q_y direction at q_z values slightly above the Yoneda peak height position (see Figure 4a for HS, Figure 4b for S, and Figure S9 for H). For a complete analysis, we also report the $I(q_y)$ cuts at the q_z values of the specular beam position for coatings of all three formulations in Figure S10, which show similar behavior.

The presence of the symmetric scattering peaks for HS and S is attributed here to the existence of a nanostructure whose in-plane characteristic correlation length/distance, $d^*(\alpha_i) = 2\pi/q^*_{y,max}$, is ∼80 nm, as estimated from the peak position along the q_y direction ($q^*_{y,max}$ = 0.078 nm^{-1} at α_i = 0.10° for both HS and S). $d^*(\alpha_i)$ seems to depend on the α_i, and it was found to increase monotonically with increasing α_i in the case of the multiphase HS coating films, but not in the case of soft S films (Figure 5). This distinct trend might imply synergy of

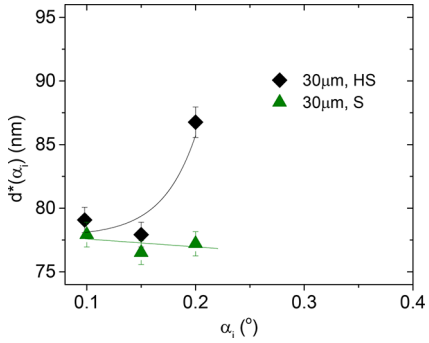

Figure 5. Heterogeneity spacing $d^*(\alpha_i)$ as a function of incident angle, α_i, for 30 μm (solid black rhombi) thick films of HS and for 30 μm (solid green triangles) S films. The lines are drawn to guide the eye. The error bar denotes the standard deviation associated with the uncertainty in determining the scattering peak positon (uncertainty in beam center determination and detector resolution) per each measurement run at a certain α_i.

shearing effects and also different net interplay of (hydrophobic, electrostatic, and hydrogen-bonding) interactions between the polymer constituents and the soluble additives due to matrix topography differences, but also different particle sintering mechanism, pointing to a more regular packing for the S sample (see the Drying-Deformation Calculations and Sintering Mechanism section). The more regular packing of the S sample is also evidenced by the presence of a second high-order scattering peak observed in Figure 4b. Conversely, the absence of higher order peaks in the $I(q_y)$ cuts reported in Figure 4a suggests a large extent of structural disorder for the HS films. Interestingly, the peak intensity is strongly enhanced and the peak shape is significantly different with respect to the analogous SAXS peak in the aqueous suspensions (see Figure 1). This difference in peak characteristics (both position and shape) between solution SAXS and GISAXS together with the disappearance of the intensity oscillations characteristic for the spherical particle shape suggests that the colloidal particles have deformed and coalesced (to some extent) during drying. We thus attribute the origin of the GISAXS scattering peaks in both HS and S films to the spatial correlation between nanostructural heterogeneities generated by incomplete particle coalescence and showing substantial electron density difference with respect to the polymer matrix. Remarkably, these nanostructural heterogeneities seem to exhibit certain directionality along the direction perpendicular to the film surface. The scattering signals for the HS and S film tend to fall on a ring but appear more focused and often elongated along the horizontal q_y direction, suggesting a preferential orientation of the scattering entities along the vertical direction (Figure 3). These rings may suggest the presence of anisotropic structures tilted throughout the plane of the film, as it will be confirmed and discussed below on the basis of GISAXS simulations. Differently from the HS and S films, the intensity oscillations typical of the particle form factor are still present for the hard non-film-forming H film, and the peaks in the respective $I(q_y)$ cuts stem from a different reason (Figure S9): they represent nanostructural spacing within a randomly packed array of noncoalesced and nondeformable hard colloids. Moreover, for the H coating, the $I(q_y)$ does not present drastic changes in curve shape as a function of increasing α_i compared to HS and S, apart from the shift in the peak structure factor (Figure S9). It should be noted that for very high α_i the signal is mostly concentrated along the specular (higher q_z) region, rather than at the Yoneda (relatively smaller q_z) refraction region, as a result of the large sample roughness (Figure S9 as compared to Figure S10c). The variable-angle GISAXS peak intensity is proportional to the amount (number and size) and the scattering length density contrast of the nanostructural heterogeneities in the coating film. According to our interpretation, larger peak intensity would imply more incomplete particle coalescence and hence less extent of chain interdiffusion between the polymer colloids, while disappearance of the scattering peak indicates a large (if not complete) degree of particle coalescence. As mentioned above, the intensity for the soft S film is ∼6 times lower than HS (Figure 3, top vs middle row). This can be understood by the expected higher degree of particle coalescence for the softer colloidal S system (see also the "GISAXS simulations" section in the Supporting Information). Notably, despite the low T_g of the S sample (Table S1), the degree of coalescence is not 100% although being larger than the one for the multiphase HS formulation. The crossover from a structured upper part to a nonstructured lower section of the film, indicated by the disappearance of the scattering peak, was found at $\alpha_i \sim 0.20°-0.25°$, corresponding to $\xi_p \approx 18$ μm (Figure S6). A significant increase of the average distance between the remaining heterogeneities $d^*(\alpha_i)$ with α_i is observed for the HS film as a result of the larger degree of particle coalescence deeper in the film (see Figure 5).

To further verify that these heterogeneities are located inside the film and not only at the air/polymer interface, we have compared the GISAXS intensity cuts with the transmitted SAXS data for free-standing HS and S sample (see Figure S11a,b). The close agreement in both intensity and form factor contribution between transmission SAXS experiments compared to the analogous GISAXS at α_i = 0.15° (nominal $\xi_p \sim 10$

DOI: 10.1021/acsapm.9b00601
ACS Appl. Polym. Mater. 2019, 1, 2482−2494

μm) confirms that these nanostructures are indeed located inside the bulk subsurface region of the coating and extend several micrometers from the surface down to the bulk of the film. Furthermore, the surface structure probed by Fourier transform of the AFM images via the power spectral density plot (see Figure S11c) is quite different from the GISAXS results, confirming that already at the lowest α_i GISAXS penetrates certain layers of particles.

To estimate the average dimension of the nanostructural heterogeneities, we attempted simulations of the GISAXS intensities. Simulation of GISAXS patterns from disordered thick films (i.e., many layers of scattering objects) in the framework of the distorted wave Born approximation[60] is a quite challenging task. We have thus opted here for simulations and fits of the horizontal $I(q_y)$ intensity cuts only (see Figure S12 and Table S3 for a summary of the extracted structural parameters) to qualitatively support the presented experimental results. The horizontally scattered intensity profile $I(q_y)$ for the H film is successfully described by an ensemble of randomly packed polydisperse spherical particles. This is expected due to the hard nature (high T_g) of the respective colloidal H particles. Conversely, the $I(q_y)$ intensity profile of soft S sample looks different and can be well described using an ensemble of narrow, vertically aligned, randomly packed cylindrical objects. The average cylinder diameter in the S film represents the average cross section of the heterogeneity domains $D_{heterog,S} \sim 8$ nm. The calculated average distance between heterogeneities is about $d^*_{S,sim} \sim 72$ nm, in agreement with the value $d^*_{S,exp} \sim 80$ nm obtained from the peak position. These simulation results are in agreement with the larger degree of coalescence of the soft S particles, leaving behind small, well-separated elongated nanodomains with a significant degree of vertical alignment. The intensity for the multiphase HS sample can be also described using a randomly packed ensemble of cylinders (see Figure S12c–e), but with an average equivalent diameter of $D_{polymer,HS} \sim 70$ nm and calculated average distance of $d^*_{HS,sim} \sim 73$ nm, in agreement with the experimentally determined average distance between heterogeneities of $d^*_{HS,exp} \sim 80$ nm. The agreement between the simulated curve and the experimental $I(q_y)$ intensity plots for the HS film is worse than for the H and the S films, suggesting that the morphology of the HS film is more complex. The simulations suggest that the scattering features in the HS film are most likely composed by partially coalesced particles with some degree of vertical alignment, leading to elongated polymeric structures. For the H and HS films, the heterogeneity domain size can be roughly estimated from the residual space between the polymer domains (interstitial space), using as input values the experimentally determined average polymer domain distance between heterogeneities of d^*_{HS}, similar to coordination of cations between anions[61] (see the "GISAXS simulations" section in the Supporting Information). The simulation results suggest thus a larger "nanoporosity" of the HS film (and of course of the H film) with respect to the S film, in agreement with the experimentally retrieved GISAXS scattering intensity. These nanostructural heterogeneities can contain nonbound material as well as some residual water. AFM tests conducted on as-prepared, water-exposed, and thoroughly rinsed S films highlight the initial presence of surfactant on both the surface and inside the film, which can be driven to the coating surface upon water exposure and eventually washed away (see Figure S13). The residual water content could be assessed by TGA analysis (see Figure S14). Interestingly, the 1% water content measured by TGA for the S film is comparable with the heterogeneities' volume fraction estimated from the GISAXS simulations ($\phi_{heterog} \approx 0.01$; see Table S3). On the contrary, the residual water content for the HS film is clearly lower than the estimated heterogeneity volume fraction ($\phi_{heterog} \approx 0.23$; see Table S3). Thus, in percentage, the heterogeneities of the S film are more filled by water than the HS heterogeneities, and the latter (HS) are more likely to be open structures filled by air (see below for further discussion). Although qualitative, these simulation results clearly show that GISAXS can capture the nanostructural difference between coatings of different chemistry/morphology and provide a rough, first, estimate of the heterogeneities size and the coating nanoporosity otherwise difficult (if not impossible) to measure with other techniques. Moreover, these heterogeneities at the nanoscale could be utilized as a predictive caliber for the performance behavior of waterborne latex coatings at the macroscopic scale. The vertical cuts $I(\alpha_f)$ vs α_f extracted from the 2D GISAXS images at similar α_i (~0.15°) for the different samples have also been analyzed and are reported in Figure S15. While both the S and HS films show evidence for a clear Yoneda peak at an exit angle of $\alpha_f \sim 0.1°$, the intensity cut of the H film only shows a broad scattering peak as a result of the large roughness and the colloidal particle nature of this film. Interestingly, the HS sample shows a second Yoneda at $\alpha_f \sim 0.07°$, suggesting that this film may contain a region with large roughness or porosity at the polymer/air interface, in contrast to the S sample. This observation is in line with the greater surface roughness of the HS film (see Figure 2). Relying on the experimental GISAXS patterns, the GISAXS simulations, and the thermogravimetry (Figure S14), we propose a schematic view of the film nanostructure (Figure 6).

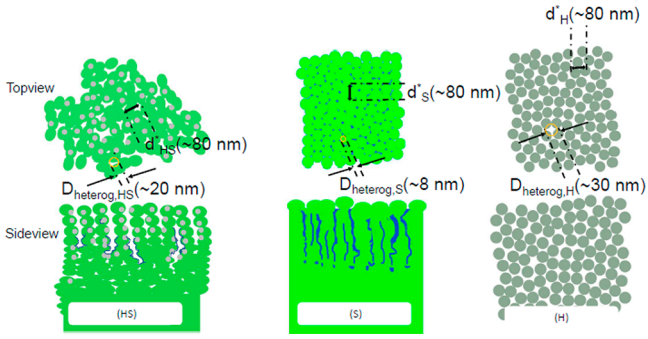

Figure 6. Envisioned—based on the experimental GISAXS patterns—nanostructures from surface overview (upper line) and side view (lower line) for left to right: the soft/hard multiphase (HS), the soft (S, $T_g \sim 5$ °C), and the hard (H, $T_g \sim 95$ °C) films. Green and gray colors denote the polymeric domains from the soft phase S and the hard phase H, respectively. The blue color in the HS and S coatings denotes the presence of residual water and other nonbound materials.

According to our vision about the coatings' nanostructure, we expect that the macroscopic barrier properties against solvent permeation[4,12] should link to the coatings' "nanoporosity" and is expected to increase as S < HS < H. To prove this conjecture, we conducted macroscopic staining tests on HS and S coatings.

Staining Experiments. Macroscopic staining tests have been conducted against wine and coffee permeation. As visible

DOI: 10.1021/acsapm.9b00601
ACS Appl. Polym. Mater. 2019, 1, 2482–2494

from Figure 7, the impact of both coffee and wine staining is much stronger for the HS coating compared to the S coating,

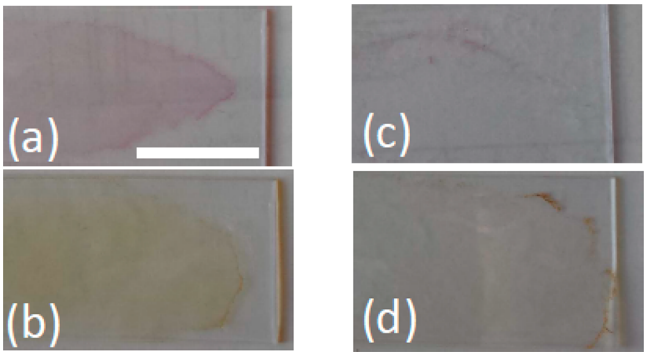

Figure 7. Macroscopic staining experiments on HS coating (left) and S coating (right): coffee stain effect (a, b); wine stain effect (c, d). For the cases of coffee and wine test, the coatings had been prepared using the aluminum slot die and after drying were kept in contact with a soaked cotton of the respective liquid for 3 h before they got macroscopically inspected. A 50 mm × 25 mm rectangular piece of cotton was soaked in the respective liquid. Scale bar: 20 mm.

suggesting a strong difference in coating barrier properties (details about these tests are reported in the Figure 7 caption).

The stronger staining effects for HS coatings agrees well with the suggested higher (open) porosity of the HS film derived by the GISAXS analysis. Thus, the presence of dispersed hard phase in the HS polymer colloid formulation from one side increases the mechanical strength and on the other hand seems to diminish their solvent-proof property[12] and to strongly enhance out-of-plane heterogeneity formation[62] compared to the single-phase soft S film.

Cross-Sectional AFM (cs-AFM). To (1) probe that the depth-resolved GISAXS trend is not technique-specific and to (2) provide additional evidence for partial coalescence, we also conducted cross-sectional AFM (cs-AFM) experiments on micrometer-sized thick films of HS on a glass substrate (Figure 8). We compare the root-mean-squared roughness (R_q) measurement as a function of distance from the air−polymer interface obtained from cs-AFM with the trend in $A(\alpha_i)$ vs α_i from GISAXS. Each individual R_q value is determined from a 2 μm × 2 μm area (dashed 2 μm × 2 μm white box, Figure 8b, upper panel) related to a 50 μm × 50 μm AFM larger micrograph as shown below. The R_q was averaged at eight different locations, at the same distance from the air−film interface, along the coating cross section. The cs-AFM results depict a monotonic decay of R_q from 8 to 3 nm with increasing distance from the air−polymer interface. This finding is in line with the experimental GISAXS evidence for structural heterogeneities vanishing from the air−polymer interface toward the glass−polymer interface. To exclude the possible presence of artifacts induced by the ion milling process, we performed a control cs-AFM experiment on a noncolloidal-based sample, namely atactic PS (M_w = 370K). The PS film (~5 μm thick) that had been thermally annealed above its T_g to repair for holes and defects exhibits negligible R_q, suggesting that possible pitfalls, if any, during the ion milling preparation of cross-sectional AFM can be safely ruled out. Thus, the results from both GISAXS and cs-AFM clearly suggest incomplete coalescence of the HS polymer colloids, with heterogeneities unevenly distributed across the film thickness. Hence, this structural anisotropy presents evidence in favor of

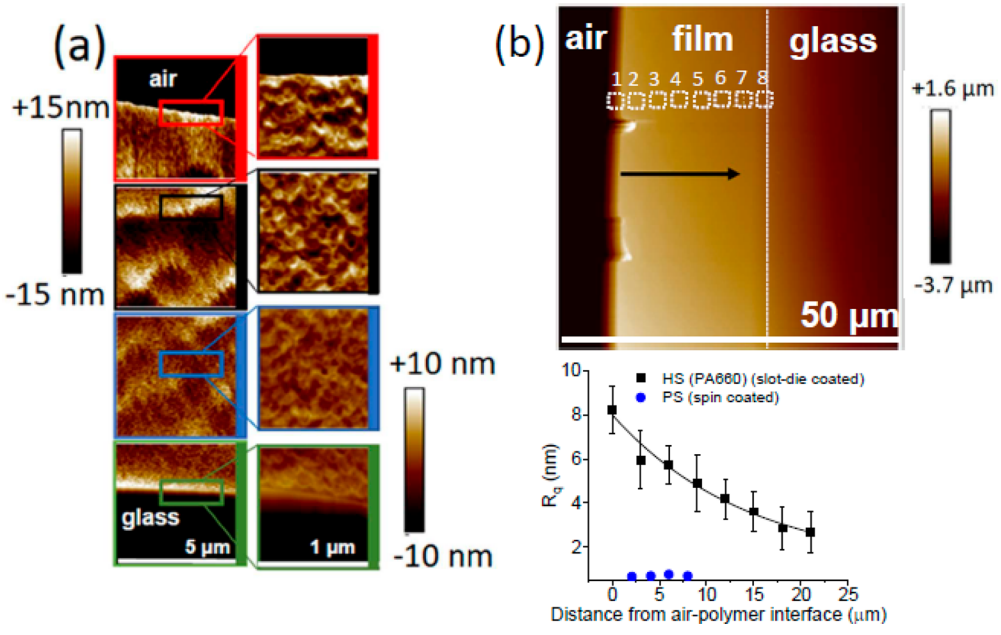

Figure 8. (a) Consecutive cross-sectional AFM micrographs (5 μm × 5 μm) from the air−film interface (top) down to the glass-film interface (bottom) for HS. Smaller (1 μm × 1 μm) boxes from the corresponding (color-matching) 5 μm × 5 μm images are also shown. (b) A 50 μm × 50 μm cross-sectional AFM image, denoting from left to right, air, HS film, and glass. The 2 μm × 2 μm white squares indicate the areas where the RMS roughness (R_q) was calculated. Estimated values of the RMS roughness (R_q) as a function of the distance from the air−polymer interface are also shown: HS (black squares) and PS (M_w = 370K) noncolloidal polymeric film prepared by spin-coating (blue circles). The error bar denotes the standard deviation of the mean R_q based on eight different locations inside the coating but measured at the same distance from the air−film interface.

DOI: 10.1021/acsapm.9b00601
ACS Appl. Polym. Mater. 2019, 1, 2482−2494

a vertical gradient in particle concentration in the HS film coatings, in agreement with simulations on latex coatings.[23]

Concerning the HS film, we speculate that the difference in RMS roughness between surface AFM ($R_{q,HS} \sim 2$ nm) and cs-AFM few micrometers below the air−surface interface ($R_{q,HS} \sim 8$ nm) could be linked to nonbound species from the emulsion polymerization that accumulate at the top surface, similarly to what observed for the S coatings (see Figure S13), although preliminary Raman data did not prove clear chemical signature of a different chemical species on top of the HS coatings. During evaporation, this (nonbound) water-soluble material including surfactant will end up in the nanovoids and can exude to the coating surface through these nanoheterogeneities.[20,63]

Solvent Exposure and Annealing. Annealing protocols are frequently employed in films of polymer colloids to reduce the amount of heterogeneities and increase resistance against solvent permeation.[31,64−66] To assess the impact of solvent annealing on the nanostructural heterogeneities, we prepared a pair of 30 μm samples (one HS coating; one S coating) which we exposed to ethanol (EtOH). Before recording GISAXS patterns, the samples had been submerged in EtOH for 1 h and then were fully dried for at least 1 h at ambient conditions. As shown in Figure 9a−d (and Figure S16), EtOH treatment has

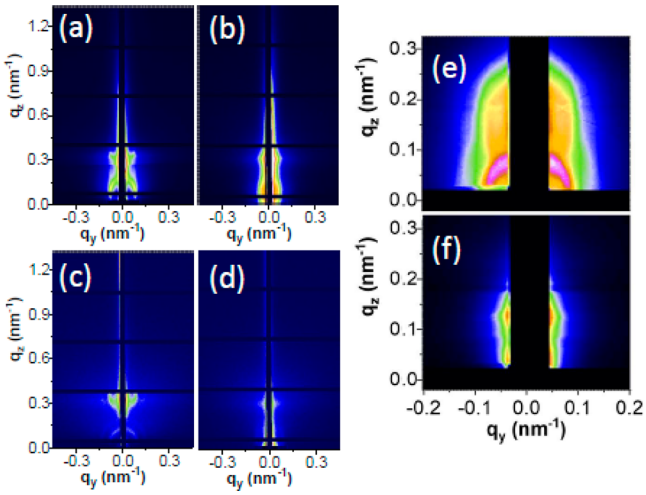

Figure 9. Annealing effects. GISAXS patterns for HS coatings before (a) and after (b) EtOH annealing at $\alpha_i = 0.2°$, with intensity scaling from 0 to 10^{-3}. GISAXS patterns for S coatings before (c) and after (d) EtOH annealing at $\alpha_i = 0.22°$, with intensity scaling from 0 to 5×10^{-4}. GISAXS patterns for an aged (12 months at ambient conditions after film preparation) HS coating before (e) and after (f) thermal annealing (T = 150 °C, 2 h) at $\alpha_i = 0.1°$, with intensity scaling from 0 to 5×10^3.

a drastic influence on the film nanostructure regardless of the presence of high T_g domains in the HS film, and the heterogeneities are smeared out upon EtOH exposure, as evidenced by loss of GISAXS signal for both HS and S films.

Weathering tests on protective coating performance include the impact of aging.[13] Interestingly, the heterogeneities are still present in a 30 μm HS coating after aging at ambient conditions for 12 months. Those heterogeneities eventually get smeared out upon thermal annealing T = 150 °C for 1 h, proven by loss of GISAXS signal for the HS film (see Figure 9e,f and Figure S16c). It is clear that thermal annealing plasticizes the film and promotes expulsion of the embedded cosolutes (water, ions, and surfactant molecules) that get entrapped in the heterogeneities.[67]

Drying-Deformation Calculations and Sintering Mechanism. The differences in nanostructure revealed by GISAXS for the three studied coating formulations may be linked to differences in the sintering mechanism. The Peclet number of the latex particles is estimated to be $Pe_{NP} = L_{wet}\dot{E}/D_{NP} \sim 4$ by considering a diffusion coefficient for the latex nanoparticles of $D_{NP} \approx 4.6 \times 10^{-12}$ m^2 s^{-1} (estimated using a water viscosity of $\mu_{water} = 8.9 \times 10^{-4}$ Pa·s at T = 23 °C and a particle radius of R_{HS} = 53 nm from DLS), an initial wet layer thickness of L_{wet} = 120 μm, and an evaporation rate $\dot{E} = (L_{wet} - L_{dry})/t_{dry} = 1.5 \times 10^{-7}$ m s^{-1}, where the wet and dry film thicknesses are L_{wet} = 120 μm and L_{dry} = 30 μm film and the drying time is $t_{dry} \sim 10$ min as estimated from the initial decay and/or stretched exponential fit in the drying curves reported in Figure S5. This large Peclet number ($Pe_{NP} > 1$), applicable for all the three investigated systems,[23] implies a much higher solvent drying rate than particle diffusion. This imbalance in transport rates leads to an uneven packing of the latex particles across the film thickness during drying.[21,23] Moreover, since the HS and S films are mostly composed by macromolecules with T_g lower than the film formation temperature, one has to consider the relative contribution of particle deformation rate with respect to solvent evaporation rate. In the framework of Routh and Russel model,[16] the parameter $\lambda = t_{def}/t_{evap} = \eta_0 R\dot{E}/(\gamma_{wa}L_{wet})$ describing the relative interplay between solvent evaporation and deformation rate of such polymer colloids can be estimated, where η is the polymer viscosity, R the particle size, $\dot{E}$ the evaporation rate, γ_{wa} is the water−air surface tension, and L_{wet} is the initial wet layer thickness. For the S coatings, the polymer (melt) viscosity can be assessed by using WLF equation for acrylic coatings.[68] At T = 23 °C, we estimate $\eta_{0,S\ melt,dry} = 1.26 \times 10^8$ Pa·s assuming a dried $T_{g,dry}$ = 278 K and $\eta_{0,S\ melt,wet} \sim 3.17 \times 10^6$ Pa·s using a wet $T_{g,wet}$ = 263 K that accounts for hydroplasticization effects[69] due to partially retained water within the coating. Thus, $\lambda_{S,wet} \sim 3 \times 10^{-3} < \lambda_{S,dry} \sim 1.1 \times 10^{-1} \ll 1$, suggesting that for the soft S coating the evaporation rate is much slower than the deformation rate. $\lambda_S \ll 1$ implies wet sintering, and together with the $Pe > 1$, a skin formation on the air−film interface of S coatings is expected.[15,16] As reported in the literature, vertical inhomogeneity in the film structure after drying could occur.[16] The large Pe (>1) could result in an uneven degree of particle coalescence, as the solvent residence time in the coating would differ across the coating cross section. Hence, the wet T_g of the particles ($T_{g,wet,S}$ = −11.8 °C),[69] in relation to the application (ambient) temperature, will dictate to what extent particles will deform in the presence of water. Hence, this coating is expected to deform considerably but more at the bottom where water is present for a longer time. Very recently, by means of Foerster resonance energy transfer (FRET) and light scattering, Johansmann et al. came to similar conclusions about a skin layer formation on the colloidal polymer film formation.[63] They proposed partial coalescence of polymer particles into polyhedral objects.[63] The same authors and others[70] also report the formation of water/surfactant arrays separating the partially deformed and soft polymer particles in their films. Their findings are in line with our proposition that the elongated nanodomains in S coatings are predominantly occupied by water as well as nonpolymeric cosolutes such as ions and surfactants (TGA and AFM results). The scattering peaks observed in our GISAXS study correlate thus with the

DOI: 10.1021/acsapm.9b00601
ACS Appl. Polym. Mater. 2019, 1, 2482−2494

center-to-center repeating distance between such heterogeneous nanodomains along the film's plane. For the HS system, using strain-controlled (strain = 0.1%; frequency ω = 1 Hz) extensional rheology on free-standing HS films (data not shown here), the HS polymer melt viscosity at T = 23 °C has been measured to be $\eta_{0,\mathrm{HS\,melt}} = 5.69 \times 10^{10}$ Pa·s. We note that this value represents an effective viscosity of the melt from the heterogeneous HS particles. The individual viscosities of each phase of the individual phases are not being used in this particular calculation. We thus find $\lambda_{HS} \sim 51$ ($>1 \gg \lambda_S$) that together with the $Pe > 1$ suggests capillary sintering ($\lambda > 10$) as the probable formation mechanism for the HS coating.[68] According to capillary sintering, the cause for deformation is capillary pressure of the liquid between the particles which induces their deformation. A capillary sintering mechanism is in good agreement with the combined GISAXS, TGA, and macroscopic staining results showing a more open porous HS coating structure at the surface compared to the S coating. It should also be considered that the presence of the hard undeformable domains in the HS particles can cause an arrest of the coalesced state earlier on during the film formation, as compared to the S system. Concerning the H coating, on account of the fact that it constitutes only of higher (compared to the film formation temperature) T_g phase, we attribute its particle deformation mechanism to dry sintering ($\eta_{0,H} \gg \eta_{0,\mathrm{HS\,melt}}$ at T = 23 °C). Indeed, a poor quality film characterized by an homogeneous distribution of nanovoids between particles is observed by GISAXS.

CONCLUSIONS

We present a detailed morphological and nanostructural investigation of industrially relevant clearcoat films from waterborne polymer colloids for paint and protective applications. The acquired results demonstrate a combined approach using X-ray scattering and microscopy to probe the quality of micrometer-sized films from waterborne polymer colloid formulations at the nanoscale level and across the film thickness. The reported nanostructural heterogeneities indicate that the particles are arrested in a partially coalesced state, well before the stage of polymer chain interdiffusion between neighboring polymer colloids. Our findings show that films from both pure soft and soft−hard multiphase polymer colloids develop nanostructural heterogeneities distributed unevenly across the film thickness and concentrated toward the air−film interface as a result of partial particle coalescence. The distribution of these heterogeneities implies vertical gradient in hydroplasticization effects having occurred earlier during film formation. Variable-angle GISAXS results have been corroborated by cross-sectional AFM. The amount of nanostructural heterogeneities was found to depend on the mechanical properties of the colloids (i.e., chemical composition), the colloidal architecture, and the film thickness. The amount and size of the nanoscale heterogeneities (a) reflect the degree of coalescence and (b) are larger for the multiphase coatings with respect to the pure soft coatings. As these heterogeneities possibly entrap surfactant molecules, residual water molecules, and ionic species from salts, their presence and their relative amount, expressed distinctly per colloid formulation, influence the coating performances in terms of both mechanical and chemical resistance against solvent penetration. The results presented here highlight the correlation between the nanostructure of waterborne coatings and the macroscopic properties such as staining behavior. Solvent and thermal annealing have been robust ways to diminish such nanostructural heterogeneities from the coating films. For certain applications such as protective coatings, these heterogeneities could be considered as defects or weak points, and thus our film post-treatment methodology provides a template on how to monitor and tune their contribution. In summary, our work presents a systematic characterization of the waterborne coating structure at the nanoscale, relevant for the optimization of industrially relevant coatings, including ink primers and paints, where film thicknesses can extend to several micrometers. The study of these nanostructures has been overlooked so far due to the lack of versatile characterization techniques that can operate in the native coating state (supported films). Moreover, our approach can be used to inspect the nanoscale morphology at large X-ray penetration depths ξ_p (up to $\alpha_i \sim 4\alpha_c$) of these high-quality films and can also be employed in the near future to perform in situ experiments on film formation from paints, adhesives, and protective coatings during drying.

ASSOCIATED CONTENT

Supporting Information

The Supporting Information is available free of charge on the ACS Publications website at DOI: 10.1021/acsapm.9b00601.

> Differential scanning calorimetry (DSC) results with heat flow curves for the examined formulations, transmission electron microscopy (TEM) on the dried HS latex particles, SAXS modeling of suspension data, film thicknesses and dependence on particle content, kinetics of film drying, scanning electron microscopy (SEM) on dried films, Stylus profilometry, calculation of penetration depth for X-rays, characteristic features of GISAXS patterns, impact of film's edge geometry, GISAXS $I(q_y)$ cuts for the H film slightly above the Yoneda position, GISAXS $I(q_y)$ cuts for the S, HS, and H films at the specular position, comparison with SAXS from free-standing HS and S films, GISAXS simulations, AFM after rinsing, thermogravimetry (TGA) results, GISAXS $I(\alpha_f)$ cuts for the S, HS, and H films at α_i = 0.15°, GISAXS $I(q_y)$ cuts for the S, HS, and H films (i) before and after EtOH annealing without aging and (ii) before/after thermal annealing on an aged sample (PDF)

AUTHOR INFORMATION

Corresponding Author

*E-mail g.portale@rug.nl.

ORCID

Giuseppe Portale: 0000-0002-4903-3159

Author Contributions

The project was conceived by G.P. The GISAXS measurements were conducted by A.V. and analyzed by A.V. and G.P. The cs-AFM experiments and the respective data analysis have been performed by Q.C. D.H.-M. assisted in the synchrotron experiments. G.t.B. assisted with the SEM measurements. Synthesis and characterization of colloids were performed in the DSM laboratories by J.S. The manuscript was written by A.V. and G.P. with the contribution of all authors. All authors have given approval to the final version of the manuscript.

DOI: 10.1021/acsapm.9b00601
ACS Appl. Polym. Mater. 2019, 1, 2482−2494

Funding
G.P. and A.V. received funding for this project by the Dutch Polymer Institute (DPI) under project 914ft16.

Notes
The authors declare no competing financial interest.

■ ACKNOWLEDGMENTS

The work of A.V. and G.P. forms part of the research programme of the Dutch Polymer Institute (DPI), project 914ft16. We thank the DUBBLE team at the ESRF and the Spanish Beamline (ALBA Synchrotron Light Source) for technical support as well as Haike Ruijters (Anton Paar) for his guidelines on zero shear viscosity measurements and Sven Broekman for support on extensional rheology measurements. Marc Stuart (RUG) is acknowledged for the TEM measurements. We also thank Jur van Dijken (RUG) for his support on TGA measurements. Ron Peters (DSM Coating Resins), Prof. Wesley Browne (RUG), and Simon Gree (IS2M, Mulhouse) are gratefully acknowledged for helpful discussions.

■ REFERENCES

(1) Mader, A.; Schirò, A.; Brischetto, M.; Pizzo, B. Interactions and Penetration of Polymers and Nanolatexes into Wood: An Overview. *Prog. Org. Coat.* **2011**, *71* (2), 123−135.
(2) Routh, A. F. Drying of Thin Colloidal Films. *Rep. Prog. Phys.* **2013**, *76* (4), 046603.
(3) van der Kooij, H. M.; Sprakel, J. Watching Paint Dry; More Exciting than It Seems. *Soft Matter* **2015**, *11* (32), 6353−6359.
(4) Martín-Fabiani, I.; Lesage de la Haye, J.; Schulz, M.; Liu, Y.; Lee, M.; Duffy, B.; D'Agosto, F.; Lansalot, M.; Keddie, J. L. Enhanced Water Barrier Properties of Surfactant-Free Polymer Films Obtained by MacroRAFT-Mediated Emulsion Polymerization. *ACS Appl. Mater. Interfaces* **2018**, *10* (13), 11221−11232.
(5) Angelova, L. V.; Ormsby, B.; Richardson, E. Diffusion of Water from a Range of Conservation Treatment Gels into Paint Films Studied by Unilateral NMR: Part I: Acrylic Emulsion Paint. *Microchem. J.* **2016**, *124*, 311−320.
(6) Hofland, A. Alkyd Resins: From down and out to Alive and Kicking. *Prog. Org. Coat.* **2012**, *73* (4), 274−282.
(7) Routh, A. F.; Keddie, J. L. *Fundamentals of Latex Film Formation*; Springer: 2010.
(8) Cardinal, C. M.; Jung, Y. D.; Ahn, K. H.; Francis, L. F. Drying Regime Maps for Particulate Coatings. *AIChE J.* **2010**, *56* (11), 2769−2780.
(9) Salamanca, J. M.; Ciampi, E.; Faux, D. A.; Glover, P. M.; McDonald, P. J.; Routh, A. F.; Peters, A. C. I. A.; Satguru, R.; Keddie, J. L. Lateral Drying in Thick Films of Waterborne Colloidal Particles. *Langmuir* **2001**, *17* (11), 3202−3207.
(10) Fortini, A.; Martín-Fabiani, I.; De La Haye, J. L.; Dugas, P.-Y.; Lansalot, M.; D'Agosto, F.; Bourgeat-Lami, E.; Keddie, J. L.; Sear, R. P. Dynamic Stratification in Drying Films of Colloidal Mixtures. *Phys. Rev. Lett.* **2016**, *116* (11), 118301.
(11) Paulis, M.; Asua, J. M. Knowledge-Based Production of Waterborne Hybrid Polymer Materials. *Macromol. React. Eng.* **2016**, *10* (1), 8−21.
(12) Yu, F.; Xu, X.; Lin, N.; Liu, X. Y. Structural Engineering of Waterborne Polyurethane for High Performance Waterproof Coatings. *RSC Adv.* **2015**, *5* (89), 72544−72552.
(13) Sbardella, F.; Pronti, L.; Santarelli, L. M.; Asua Gonzàlez, M. J.; Bracciale, P. M. Waterborne Acrylate-Based Hybrid Coatings with Enhanced Resistance Properties on Stone Surfaces. *Coatings* **2018**, *8*, 283.
(14) Overbeek, A. Polymer Heterogeneity in Waterborne Coatings. *J. Coatings Technol. Res.* **2010**, *7* (1), 1.
(15) Routh, A. F.; Russel, W. B. A Process Model for Latex Film Formation: Limiting Regimes for Individual Driving Forces. *Langmuir* **1999**, *15* (22), 7762−7773.
(16) Routh, A. F.; Russel, W. B. Deformation Mechanisms during Latex Film Formation: Experimental Evidence. *Ind. Eng. Chem. Res.* **2001**, *40* (20), 4302−4308.
(17) Nassar, M.; Gromer, A.; Thalmann, F.; Hébraud, P.; Holl, Y. Velocity of Lateral Drying Fronts in Film Formation by Drying of Colloidal Dispersions. A 2D Simulation. *J. Colloid Interface Sci.* **2018**, *511*, 424−433.
(18) Gorce, J.-P.; Bovey, D.; McDonald, P. J.; Palasz, P.; Taylor, D.; Keddie, J. L. Vertical Water Distribution during the Drying of Polymer Films Cast from Aqueous Emulsions. *Eur. Phys. J. E: Soft Matter Biol. Phys.* **2002**, *8* (4), 421−429.
(19) Liu, Y.; Gajewicz, A. M.; Rodin, V.; Soer, W.-J.; Scheerder, J.; Satgurunathan, G.; McDonald, P. J.; Keddie, J. L. Explanations for Water Whitening in Secondary Dispersion and Emulsion Polymer Films. *J. Polym. Sci., Part B: Polym. Phys.* **2016**, *54* (16), 1658−1674.
(20) Arnold, C.; Thalmann, F.; Marques, C.; Marie, P.; Holl, Y. Surfactant Distribution in Waterborne Acrylic Films. 1. Bulk Investigation. *J. Phys. Chem. B* **2010**, *114* (28), 9135−9147.
(21) Mallégol, J.; Gorce, J.-P.; Dupont, O.; Jeynes, C.; McDonald, P. J.; Keddie, J. L. Origins and Effects of a Surfactant Excess near the Surface of Waterborne Acrylic Pressure-Sensitive Adhesives. *Langmuir* **2002**, *18* (11), 4478−4487.
(22) Belaroui, F.; Cabane, B.; Dorget, M.; Grohens, Y.; Marie, P.; Holl, Y. Small-Angle Neutron Scattering Study of Particle Coalescence and SDS Desorption during Film Formation from Carboxylated Acrylic Latices. *J. Colloid Interface Sci.* **2003**, *262* (2), 409−417.
(23) Gromer, A.; Thalmann, F.; Hébraud, P.; Holl, Y. Simulation of Vertical Surfactant Distributions in Drying Latex Films. *Langmuir* **2017**, *33* (2), 561−572.
(24) Carter, F. T.; Kowalczyk, R. M.; Millichamp, I.; Chainey, M.; Keddie, J. L. Correlating Particle Deformation with Water Concentration Profiles during Latex Film Formation: Reasons That Softer Latex Films Take Longer to Dry. *Langmuir* **2014**, *30* (32), 9672−9681.
(25) Ballauff, M.; Bolze, J.; Dingenouts, N.; Hickl, P.; Pötschke, D. Small-Angle X-Ray Scattering on Latexes. *Macromol. Chem. Phys.* **1996**, *197* (10), 3043−3066.
(26) Dingenouts, N.; Bolze, J.; Pötschke, D.; Ballauff, M. Analysis of Polymer Latexes by Small-Angle X-Ray Scattering BT - Polymer Latexes - Epoxide Resins - Polyampholytes; Springer Berlin Heidelberg: Berlin. *Heidelberg* **1999**, *144*, 1−47.
(27) Ballauff, M. Analysis of Polymer Colloids by Small-Angle X-Ray and Neutron Scattering: Contrast Variation. *Adv. Eng. Mater.* **2011**, *13* (8), 793−802.
(28) Yoo, J. N.; Sperling, L. H.; Glinka, C. J.; Klein, A. Characterization of Film Formation from Polystyrene Latex Particles via SANS. 2. High Molecular Weight. *Macromolecules* **1991**, *24* (10), 2868−2876.
(29) Dingenouts, N.; Ballauff, M. Assessment of Spatial Order in Dried Latexes by Small-Angle X-Ray Scattering. *Macromolecules* **1998**, *31* (21), 7423−7429.
(30) Dingenouts, N.; Ballauff, M. First Stage of Film Formation by Latexes Investigated by Small-Angle X-Ray Scattering. *Langmuir* **1999**, *15* (9), 3283−3288.
(31) Nawaz, Q.; Rharbi, Y. Various Modes of Void Closure during Dry Sintering of Close-Packed Nanoparticles. *Langmuir* **2010**, *26* (2), 1226−1231.
(32) Crowley, T. L.; Sanderson, A. R.; Morrison, J. D.; Barry, M. D.; Morton-Jones, A. J.; Rennie, A. R. Formation of Bilayers and Plateau Borders during the Drying of Film-Forming Latexes as Investigated by Small-Angle Neutron Scattering. *Langmuir* **1992**, *8* (9), 2110−2123.
(33) Joanicot, M.; Wong, K.; Richard, J.; Maquet, J.; Cabane, B. Ripening of Cellular Latex Films. *Macromolecules* **1993**, *26* (12), 3168−3175.
(34) Joanicot, M.; Wong, K.; Cabane, B. Interdiffusion in Cellular Latex Films. *Macromolecules* **1996**, *29* (14), 4976−4984.

DOI: 10.1021/acsapm.9b00601
ACS Appl. Polym. Mater. 2019, 1, 2482−2494

(35) Ding, X.; Liu, J.; Harris, T. A. L. A Review of the Operating Limits in Slot Die Coating Processes. *AIChE J.* **2016**, *62* (7), 2508−2524.
(36) Hu, S.; Rieger, J.; Roth, S. V.; Gehrke, R.; Leyrer, R. J.; Men, Y. GIUSAXS and AFM Studies on Surface Reconstruction of Latex Thin Films during Thermal Treatment. *Langmuir* **2009**, *25* (7), 4230−4234.
(37) Müller-Buschbaum, P. *High-Resolution Grazing Incidence Small Angle X-Ray Scattering: Investigation of Micrometer Sized Structured Polymer Films BT - Characterization of Polymer Surfaces and Thin Films*; Grundke, K., Stamm, M., Adler, H.-J., Eds.; Springer: Berlin, 2006; pp 23−32.
(38) Busch, P.; Posselt, D.; Smilgies, D.-M.; Rauscher, M.; Papadakis, C. M. Inner Structure of Thin Films of Lamellar Poly(Styrene-b-Butadiene) Diblock Copolymers As Revealed by Grazing-Incidence Small-Angle Scattering. *Macromolecules* **2007**, *40* (3), 630−640.
(39) Zhang, J.; Posselt, D.; Smilgies, D.-M.; Perlich, J.; Kyriakos, K.; Jaksch, S.; Papadakis, C. M. Lamellar Diblock Copolymer Thin Films during Solvent Vapor Annealing Studied by GISAXS: Different Behavior of Parallel and Perpendicular Lamellae. *Macromolecules* **2014**, *47* (16), 5711−5718.
(40) Gu, X.; Gunkel, I.; Hexemer, A.; Russell, T. P. Controlling Domain Spacing and Grain Size in Cylindrical Block Copolymer Thin Films by Means of Thermal and Solvent Vapor Annealing. *Macromolecules* **2016**, *49* (9), 3373−3381.
(41) Posselt, D.; Zhang, J.; Smilgies, D.-M.; Berezkin, A. V.; Potemkin, I. I.; Papadakis, C. M. Restructuring in Block Copolymer Thin Films: In Situ GISAXS Investigations during Solvent Vapor Annealing. *Prog. Polym. Sci.* **2017**, *66*, 80−115.
(42) Ferrarese Lupi, F.; Giammaria, T. J.; Seguini, G.; Laus, M.; Dubček, P.; Pivac, B.; Bernstorff, S.; Perego, M. GISAXS Analysis of the In-Depth Morphology of Thick PS-b-PMMA Films. *ACS Appl. Mater. Interfaces* **2017**, *9* (12), 11054−11063.
(43) Chen, Q.; Scheerder, J.; de Vos, K.; Tak, R. Influence of Cosolvent Retention on Film Formation and Surface Mechanical Properties of Water Based Acrylic Coatings by Atomic Force Microscopy. *Prog. Org. Coat.* **2017**, *102*, 231−238.
(44) Stevens, J. R.; Mao, A. C. Glass Transition of Atactic Polystyrene by Ortho-Positronium Decay. *J. Appl. Phys.* **1970**, *41* (11), 4273−4275.
(45) Borsboom, M.; Bras, W.; Cerjak, I.; Detollenaere, D.; Glastra van Loon, D.; Goedtkindt, P.; Konijnenburg, M.; Lassing, P.; Levine, Y.; Munneke, B.; Oversluizen, M.; Van Tol, R.; Vlieg, E. The Dutch−Belgian Beamline at the ESRF. *J. Synchrotron Radiat.* **1998**, *5* (3), 518−520.
(46) Portale, G.; Cavallo, D.; Alfonso, G. C.; Hermida-Merino, D.; van Drongelen, M.; Balzano, L.; Peters, G. W. M.; Goossens, J. G. P.; Bras, W. Polymer Crystallization Studies under Processing-Relevant Conditions at the SAXS/WAXS DUBBLE Beamline at the ESRF. *J. Appl. Crystallogr.* **2013**, *46* (6), 1681−1689.
(47) Yoneda, Y. Anomalous Surface Reflection of X Rays. *Phys. Rev.* **1963**, *131* (5), 2010−2013.
(48) Guinier, A.; Fournet, G. *Small-Angle Scattering of X-Rays*; John Wiley & Sons: New York, 1955.
(49) Bolze, J.; Ballauff, M.; Kijlstra, J.; Rudhardt, D. Application of Small-Angle X-Ray Scattering as a Tool for the Structural Analysis of Industrial Polymer Dispersions. *Macromol. Mater. Eng.* **2003**, *288* (6), 495−502.
(50) Bolze, J.; Ballauff, M. Study of Spatial Inhomogeneities in Swollen Latex Particles by Small-Angle X-Ray Scattering: The Wall-Repulsion Effect Revisited. *Macromolecules* **1995**, *28* (22), 7429−7433.
(51) Sahir Arıkan, M. A.; Balkan, T. Process Modeling, Simulation, and Paint Thickness Measurement for Robotic Spray Painting. *J. Robot. Syst.* **2000**, *17* (9), 479−494.
(52) Maier, F.; Zagar, B. G. Measurement of Paint Coating Thickness by Thermal Transient Method. *IEEE Trans. Instrum. Meas.* **2009**, *58* (6), 1958−1966.
(53) Müller-Buschbaum, P. GISAXS and GISANS as Metrology Technique for Understanding the 3D Morphology of Block Copolymer Thin Films. *Eur. Polym. J.* **2016**, *81*, 470−493.
(54) Babonneau, D.; Naudon, A.; Thiaudière, D.; Lequien, S. Morphological Characterization of Ion-Sputtered C−Ag, C/C−Ag and Ag/C Films by GISAXS. *J. Appl. Crystallogr.* **1999**, *32* (2), 226−233.
(55) Singh, M. A.; Groves, M. N. Depth Profiling of Polymer Films with Grazing-Incidence Small-Angle X-Ray Scattering. *Acta Crystallogr., Sect. A: Found. Crystallogr.* **2009**, *65* (3), 190−201.
(56) Okuda, H.; Takeshita, K.; Ochiai, S.; Sakurai, S.; Kitajima, Y. Near-Surface Relaxation Structure of Annealed Block Copolymer Film on Si Substrates Examined by Grazing-Incidence Small-Angle Scattering Utilizing Soft X-Rays. *J. Appl. Crystallogr.* **2011**, *44* (2), 380−384.
(57) Vineyard, G. H. Grazing-Incidence Diffraction and the Distorted-Wave Approximation for the Study of Surfaces. *Phys. Rev. B: Condens. Matter Mater. Phys.* **1982**, *26* (8), 4146−4159.
(58) Buffet, A.; Abul Kashem, M. M.; Perlich, J.; Herzog, G.; Schwartzkopf, M.; Gehrke, R.; Roth, S. V. Stripe-Like Pattern Formation in Airbrush-Spray Deposition of Colloidal Polymer Film. *Adv. Eng. Mater.* **2010**, *12* (12), 1235−1239.
(59) Altamura, D.; Holý, V.; Siliqi, D.; Lekshmi, I. C.; Nobile, C.; Maruccio, G.; Cozzoli, P. D.; Fan, L.; Gozzo, F.; Giannini, C. Exploiting GISAXS for the Study of a 3D Ordered Superlattice of Self-Assembled Colloidal Iron Oxide Nanocrystals. *Cryst. Growth Des.* **2012**, *12* (11), 5505−5512.
(60) Lazzari, R.; Leroy, F.; Renaud, G. Grazing-Incidence Small-Angle x-Ray Scattering from Dense Packing of Islands on Surfaces: Development of Distorted Wave Born Approximation and Correlation between Particle Sizes and Spacing. *Phys. Rev. B: Condens. Matter Mater. Phys.* **2007**, *76* (12), 125411.
(61) Nho, H. W.; Yoon, T. H. Structural Colour of Unary and Binary Colloidal Crystals Probed by Scanning Transmission X-Ray Microscopy and Optical Microscopy. *Sci. Rep.* **2017**, *7* (1), 12424.
(62) Liu, X.; Liu, W.; Carr, A. J.; Santiago Vazquez, D.; Nykypanchuk, D.; Majewski, P. W.; Routh, A. F.; Bhatia, S. R. Stratification during Evaporative Assembly of Multicomponent Nanoparticle Films. *J. Colloid Interface Sci.* **2018**, *515*, 70−77.
(63) Wahdat, H.; Hirth, C.; Johannsmann, D.; Gerst, M.; Rückel, M.; Adams, J. Film Formation of Pressure-Sensitive Adhesives (PSAs) Studied with Förster Resonance Energy Transfer (FRET) and Scattering Intensity. *Macromolecules* **2018**, *51* (12), 4718−4726.
(64) Goudy, A.; Gee, M. L.; Biggs, S.; Underwood, S. Atomic Force Microscopy Study of Polystyrene Latex Film Morphology: Effects of Aging and Annealing. *Langmuir* **1995**, *11*, 4454.
(65) Colombini, D.; Hassander, H.; Karlsson, O. J.; Maurer, F. H. J. Effects of Thermal Annealing on the Viscoelastic Properties and Morphology of Bimodal Hard/Soft Latex Blends. *J. Polym. Sci., Part B: Polym. Phys.* **2005**, *43* (17), 2289−2306.
(66) Liu, X.; Zhao, D.; Geng, C.; Zhang, L.; Tan, T.; Hu, M.; Yan, Q. Fabrication of Colloidal Photonic Crystal Heterostructures Free of Interface Imperfection Based on Solvent Vapor Annealing. *J. Colloid Interface Sci.* **2014**, *434*, 98−103.
(67) Hu, S.; Rieger, J.; Yi, Z.; Zhang, J.; Chen, X.; Roth, S. V.; Gehrke, R.; Men, Y. Structural Evolution of a Colloidal Crystal Fiber during Heating and Annealing Studied by in Situ Synchrotron Small Angle X-Ray Scattering. *Langmuir* **2010**, *26* (16), 13216−13220.
(68) Gonzalez, E.; Paulis, M.; Barandiaran, M. J.; Keddie, J. L. Use of a Routh−Russel Deformation Map To Achieve Film Formation of a Latex with a High Glass Transition Temperature. *Langmuir* **2013**, *29* (6), 2044−2053.
(69) Tsavalas, J. G.; Sundberg, D. C. Hydroplasticization of Polymers: Model Predictions and Application to Emulsion Polymers. *Langmuir* **2010**, *26* (10), 6960−6966.
(70) Martín-Fabiani, I.; Makepeace, D. K.; Richardson, P. G.; Lesage de la Haye, J.; Venero, D. A.; Rogers, S. E.; D'Agosto, F.; Lansalot, M.; Keddie, J. L. In Situ Monitoring of Latex Film Formation by Small-Angle Neutron Scattering: Evolving Distributions of Hydro-

DOI: 10.1021/acsapm.9b00601
ACS Appl. Polym. Mater. 2019, 1, 2482−2494

philic Stabilizers in Drying Colloidal Films. *Langmuir* **2019**, 35 (10), 3822−3831.

DOI: 10.1021/acsapm.9b00601
ACS Appl. Polym. Mater. 2019, 1, 2482−2494